RUNNING LATE: EXPLORING THE DELAYED SUPERMASSIVE BLACK HOLE GROWTH SEEN BY HYDRO-DYNAMICAL SIMULATIONS

An Undergraduate Research Scholars Thesis

by

MEGAN TAYLOR TILLMAN

Submitted to the Undergraduate Research Scholars Program at
Texas A&M University
in partial fulfillment of the requirements for the designation as an

UNDERGRADUATE RESEARCH SCHOLAR

Approved by Research Advisors:

Dr. Louis Strigari
Dr. Kim-Vy Tran
Dr. Claude-André Faucher-Giguère
Dr. Sarah Wellons
Dr. Luke Zoltan Kelley

May 2020

Major: Physics

TABLE OF CONTENTS

Page

ABSTRACT 1

ACKNOWLEDGMENTS 3

NOMENCLATURE 4

SECTION

I. INTRODUCTION 5

II. METHODS 7

- Known Relations 8
- Simulation Motivated Models 9
- Mathematical Pipeline 14
- Statistical Extractions 17

III. RESULTS 22

- The Predicted QLF 22
- The Duty Cycle and Average Specific Black Hole Accretion Rate 24
- Best Fit Parameters 25

IV. DISCUSSION 30

- The Free Parameters 30
- On the Lack of Low Luminosity Quasar Detection 31

V. CONCLUSION 34

REFERENCES 36

ABSTRACT

Running Late: Exploring the Delayed Supermassive Black Hole Growth Seen by Hydro-Dynamical Simulations

Megan Taylor Tillman
Department of Physics and Astronomy
Texas A&M University

Research Advisor: Dr. Louis Strigari
Department of Physics and Astronomy
Texas A&M University

Research Advisor: Dr. Kim-Vy Tran
Department of Physics and Astronomy
University of New South Wales

Research Advisors: Dr. Claude-André Faucher-Giguère,
Dr. Sarah Wellons
Dr. Luke Zoltan Kelley
Department of Physics and Astronomy
Northwestern University

Despite the vast amount of processes that depend on the co-evolution of supermassive black holes (SMBHs) and their host galaxies, their physical relationship is still not fully understood. Observations have revealed a well-constrained scaling relation between SMBH mass and galaxy bulge mass in the local universe. In galaxy formation simulations, a different form of SMBH growth behavior emerges at high redshift: prolonged slow growth in the early universe followed by coherent fueling that results in a rapid increase in the central BH's mass. After this "catch-up" period of rapid growth, the SMBH growth resembles the well documented observed local scaling relation between SMBH mass and galaxy bulge mass. We conduct an in-depth study of these SMBH growth behaviors to explore implications it has on the early universe scaling relation.

We construct a simple model, using said behaviors, to predict the quasar luminosity func-

tion which can be compared to well-documented observable quantities. To combine the simulation behaviors with a mock catalog of galaxies, we employ mathematical convolution techniques. This involves numerical integration methods over a population of dark matter halos and various models that relate the dark matter halo population to quasar luminosity. The models this study produces to resemble the simulation behaviors contains three free parameters. Thus, we employ a least squares fit method on a three dimensional parameter space to find the free parameters that best fit the predictions of our study to various observational data. These results allow us to systematically quantify the range of allowed scenarios for the emergence of the scaling relation between SMBH mass and galaxy bulge mass observed in the local universe.

ACKNOWLEDGMENTS

This project began as part of the Northwestern CIERA (Center for Interdisciplinary Exploration and Research in Astrophysics) Research Experience for Undergraduates Program. As I continued my undergraduate degree at Texas A&M University, work on this project has only been able to continue due to the support of Dr. Claude-André Faucher-Giguère's research group over the past two years. Along with Dr. Claude-André Faucher-Giguère, I specifically want to thank: Dr. Sarah Wellons, Dr. Luke Zoltan Kelley, Dr. Jonathan Stern, Dr. Alexander Richings, Dr. Daniel Anglés-Alcázar, Alexander Gurvich, Zachary Hafen, and Lindsey Byrne.

I want to thank Dr. Kim-Vy Tran and Dr. Louis Strigari for being my local advisors at Texas A&M University, and for being available to advise me on this thesis.

I also thank my parents, Jason and Amy, and my siblings, Jack and Katelyn, for supporting my ambitions to pursue a career in the field of astrophysics.

This material is based upon work supported by NSF Grant No. AST-1757792.

NOMENCLATURE

SMBH	Supermassive Black Hole
BH	Black Hole
FIRE	Feedback In Realistic Environments
AGN	Active Galactic Nuclei
QLF	Quasar Luminosity Function
HMF	Halo Mass Function
SMF	Stellar Mass Function
SMHM	Stellar Mass Halo Mass
UM	Universe Machine
PDF	Probability Distribution Function
sSFR	specific Star Formation Rate
SMBHMF	Supermassive Black Hole Mass Function
η	Eddington Ratio
z	redshift

SECTION I

INTRODUCTION

In recent years, numerous cosmological simulations have been developed and continuously improved on such as Illustris, EAGLE, and RAMSES ([1, 2, 3] respectively). The goal, of these theoretical simulations, is to explore the long-timescale processes of the universe, motivated by current understanding of physics, to stimulate findings that may be impossible to discover through observation alone. The FIRE (Feedback In Realistic Environments) project aims to create more detailed galaxy evolution simulations focusing on small scale processes, like feedback (stellar winds, supernovae etc.), and their effects on the growth of galaxies [4, 5].

Observations indicate a well-constrained scaling relation between the supermassive black hole mass and galaxy bulge mass in the local universe (for overview and example studies see [6, 7, 8]), but astronomers know little about what the scaling relation may look like in the early universe. The optimal way to approach this problem may be through a study of galaxy evolution simulations to provide insight complementary to where observational techniques are limited.

Comparing predictions to observable quantities is essential in any theoretical study but can be a difficult task. Direct measurements of galaxy bulge mass or a galaxy's central black hole are exceedingly challenging. An elegant solution to this problem is the indirect comparison to an observable with vast amounts of data available across a large time-scale. Quasars are one example of a fairly well documented observable. Quasars are extremely energetic and thus easy to detect; quasars are the most energetic form of active galactic nuclei (AGN), an event resulting from a SMBH taking on mass, and are a source of feedback within a galaxy. Feedback from SMBHs appears to be the main "missing ingredient" in understanding the origin of "red and dead" elliptical galaxies (elliptical galaxies no longer forming stars), which is arguably the biggest open question in galaxy formation theory.

The behavior of the SMBH evolution in the FIRE simulations consistently produces a unique co-evolution between the SMBH and its host galaxy's bulge mass (see [9, 10] for review). This begins with prolonged slow growth in the early universe which is followed by a rapid increase in mass. As discussed in [10], the rapid increase in mass is consistently seen to begin at some critical bulge mass of $\sim 10^{10}\mathrm{M}_{\odot}$. Finally an approach and eventual fall onto the SMBH mass galaxy bulge mass local scaling relation is predicted. The delayed rapid growth of the SMBH is the focus of our study. This growth behavior represents a scenario for the emergence of the SMBH mass - bulge mass scaling relation that we wish to quantify.

Within our study, we analyze how the delayed supermassive black hole growth, predicted by FIRE simulations, compares to observational data. We explore the implications this growth behavior has on an early universe scaling relation. To test this more thoroughly we construct a model, based on the predicted growth behavior, to compare to observables. As mentioned above, quasars are some of the brightest objects and an ideal observable to compare to for SMBH-related studies. Thus, we predict the quasar luminosity function (QLF) describing the number density of quasars as a function of luminosity and redshift (z). Our predicted QLF agrees with observational QLF data up to $z = 4$ with fairly well constrained, and physically reasonable, free parameters.

The layout of this paper will be as follows: SECTION II will describe the details of our model through both the relations we establish (**Known Relations** and **Simulation Motivated Models**) and the calculations required to convolve them (**Mathematical Pipeline**). We lay out the results of our model in SECTION III, discuss implications in SECTION IV, and summarize our main conclusions in SECTION V.

SECTION II

METHODS

To construct the QLF we produce a cosmological population of quasars by convolving the known statistics of galaxy populations (e.g., the halo mass function) with the SMBH growth behavior predicted by simulations. This involves numerical integration methods over a population of dark matter halos and several relations to connect dark matter halo mass, stellar mass, and SMBH mass to quasar luminosity.

Of the relations utilized, the stellar mass SMBH mass relation and the SMBH accretion rate model are directly motivated by the FIRE simulation behaviors this study aims to explore (see **Simulation Motivated Models**). We see two growth behaviors. First the galaxy stellar mass and central BH grow slowly in the early universe and accretion events tend to be scattered. Once the galactic disk forms we begin to see the second growth behavior of more coherent fueling of the central BH and an eventual fall onto the observed local scaling relation discussed in [7] and similar studies. Both of these growth behaviors are modeled mathematically in two eras: a ‘pre-disk’ and ‘post-disk’ era. Which era we conduct calculations in is determined based on a host galaxy’s stellar mass.

The pre-disk era is before the organization/settlement of a galactic disk. This era consists of slow SMBH growth fed by sporadic inconsistent accretion events.

The post-disk era occurs after the formation of a galactic disk and is when the SMBH gains the majority of its mass. To resemble the critical bulge mass seen in [10], the pre-disk era ends and post-disk begins once the host galaxy’s stellar mass hits some critical threshold we dub $M_{*\mathrm{crit}}$.

The post-disk era consists of more consistent SMBH accretion events and demonstrates two growth behaviors: rapid growth due to the undermassive BH at the start of era, followed by growth that falls onto the local scaling relation (using the local slope from [7]). Both of these growth behaviors are achieved through a simple mathematical model of proportional growth rates between SMBH mass and galaxy stellar mass (see *Universal Supermassive Black Hole Accretion Model* for more details).

All other relations are empirically-motivated using known scaling relations (e.g., the star formation sequence) or results from dark-matter-only simulations (e.g., the halo mass function). These known relations are described throughout **Known Relations**. When applicable, the free parameters of these observational relations are chosen to be consistent with the FIRE simulations, along with any other applicable relations, to ensure self-consistency of our study. We discuss these free parameters, along with our choices for them, within each relations' corresponding sub-sections throughout **Known Relations** and **Simulation Motivated Models**.

The formulations of our calculations are discussed throughout **Mathematical Pipeline**. A discussion on how the relations are implemented is conducted whenever each individual relation is required. Some relations are utilized in multiple calculations for different purposes; we discuss specifics on the implementation each time. Formulations represented as integrals are carried through numerically unless otherwise mentioned. Each integration is conducted over a range deemed physically reasonable. These details are discussed further in appropriate sub-sections within **Mathematical Pipeline**.

Known Relations

Halo Mass Function

The Halo Mass Function (HMF) quantifies the number density of halo masses as a function of redshift ($\frac{d\mathrm{N}}{d\ln \mathrm{M_H}}\,(\mathrm{M_H}, z)$) for a given cosmology. For our model we use Colossus, a public, open-source python package for calculations related to cosmology, the large-scale structure of matter in the universe, and the properties of dark matter halos [11].

We generate a HMF using the Despali mass function model [12], as a function of virial mass, assuming a Planck 2015 cosmology. The Despali halo mass function was chosen because it covers the full range of redshifts we seek to study ($z = 0 - 4$) and we utilize a virial mass definition for the halo mass for consistency with the stellar mass - halo mass relation described in *Stellar Mass - Halo Mass Relation*. The Planck 15 parameters use a ΛCDM model and can be found in [13] table 4, column 6. The Planck 2015 parameters were chosen for consistency with the other cosmological relations we employ, however we note that updating to the Planck 2018 parameters does not significantly change the results of our study.

Stellar Mass - Halo Mass Relation

We establish the redshift dependent stellar mass - halo mass (SMHM) relation using Universe Machine (UM) [14]. UM provides a ratio between median stellar mass and peak halo mass utilizing the halo's star formation history ($\mathrm{M}_{*}\left(\mathrm{M}_{\mathrm{H}}, z\right)$). We utilize this for a direct conversion between stellar mass and halo mass and for the calculation of the slope of that relation at any given point.

We set the SMHM relation scatter to $\sigma_{\ln \mathrm{M}_{*}} = 0.7$ dex. In [14] §4.2.2. scatter on this relation is explored thoroughly. We find our overall findings are not impacted by small variations in this scatter.

Simulation Motivated Models

Stellar Mass - Supermassive Black Hole Mass Relation

As previously discussed, the relationship between stellar mass and SMBH mass ($\mathrm{M}_{*} - \mathrm{M}_{\mathrm{BH}}$) is motivated by the behaviors exhibited in the FIRE simulations. It is modeled through two distinct growth behaviors differing between the pre- and post-disk eras and separated by some critical stellar mass $\mathrm{M}_{*\mathrm{crit}}$.

We know that in the pre-disk era the SMBH is undermassive and grows slowly therefore we model this relation as the power law

$$\log_{10} \mathrm{M}_{\mathrm{BH}} = a \log_{10} \mathrm{M}_{*} + b. \qquad \text{(Eq. 1)}$$

The slope of the power law, a, is chosen to be 0.2, to represent the slow growth of the SMBH in this era. We find that small variations in this slope does not significantly change the results of our predicted QLF. The intercept, b, is a normalization constant defined to ensure the overall relationship is continuous at the point the two eras meet.

In the post-disk era, the galaxy is able to fuel the central BH at a rate proportional to the galaxy's stellar mass growth. After an initial transition period of rapid growth, this manifests observationally as the known local scaling relation between SMBH mass and galaxy bulge mass [7]. We implement this local scaling relation as

$$\frac{d\log \mathrm{M_{BH}}}{d\log \mathrm{M_*}} \approx 1, \tag{Eq. 2}$$

where we approximate their slope (which is closer to 1.12) as 1 for the sake of simplicity.

We thus model the post-disk era growth through

$$\dot{\mathrm{M}}_{\mathrm{BH}} = \alpha \dot{\mathrm{M}}_*^{\beta}, \tag{Eq. 3}$$

from which β is equivalent to Eq. 2 and is the slope for which the relation approaches asymptotically. The value for α is calculated using β, $\mathrm{M_{*crit}}$, and a mass pair normalization point $(\mathrm{M_*} = 10^{11}\mathrm{M_\odot}, \mathrm{M_{BH}} = 10^{8.2}\mathrm{M_\odot})$. The normalization point was chosen to resemble that chosen in [7].

In log space, Eq. 3 takes the form

$$\frac{d\log \mathrm{M_{BH}}}{d\log \mathrm{M_*}} = \alpha\beta \frac{\mathrm{M}_*^{\beta}}{\mathrm{M_{BH}}}, \tag{Eq. 4}$$

such that the relation between stellar mass and black hole mass is

$$\log \mathrm{M_{BH}} = \log \left[\mathrm{M_{BHcrit}} + \alpha \mathrm{M}_*^{\beta-1} \left(\mathrm{M_*} - \mathrm{M_{*crit}}\right)\right] \tag{Eq. 5}$$

at $\mathrm{M_*} > \mathrm{M_{*crit}}$. Examples of the $\mathrm{M_*} - \mathrm{M_{BH}}$ evolution for different $\mathrm{M_{*crit}}$ values can be seen in Figure 1.

Within the framework of this model, different choices for $\mathrm{M_{*crit}}$ can result in more or less undermassive BHs as the post-disk era is initialized; this behavior will affect the initial growth rate of the central BH as era begins, but the overall behavior between the two will remain the same. Decreasing $\mathrm{M_{*crit}}$ will just cause the post-disk era to be triggered sooner which results in

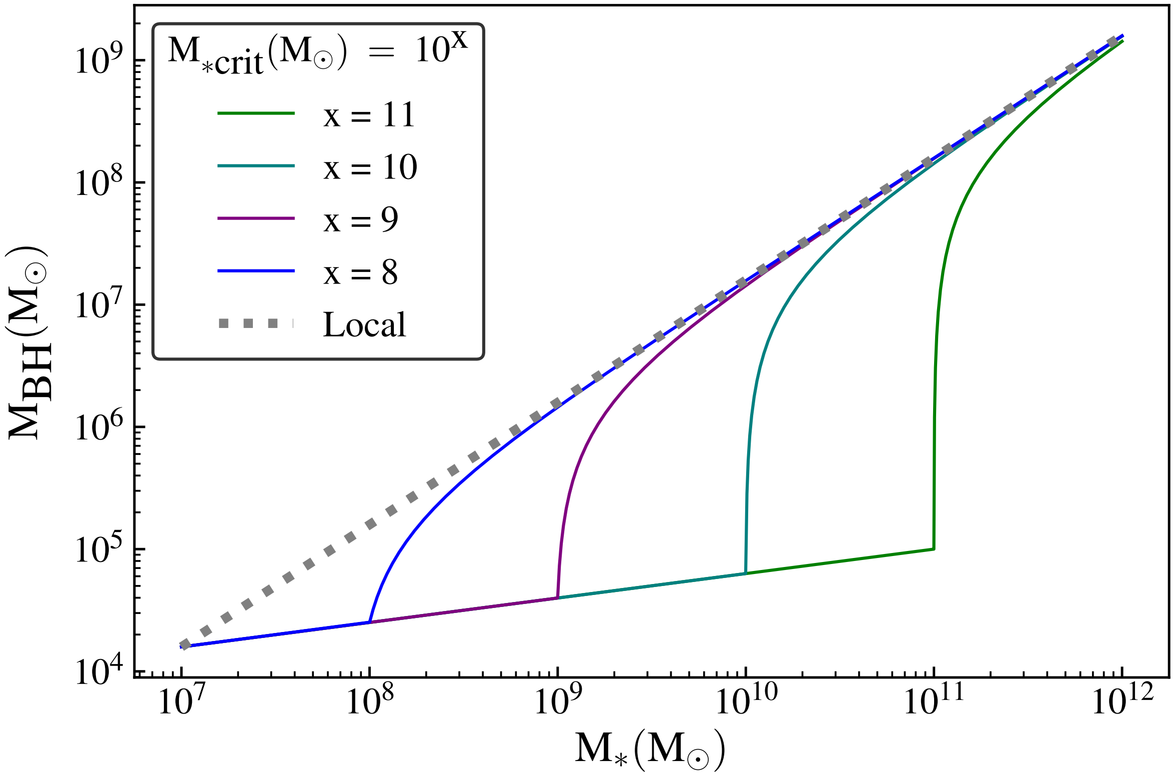

Figure 1: Stellar mass - SMBH mass relation for varying M_{*crit}. The pre-disk era corresponds to the shallow linear slope. The post-disk era corresponds to the asymptotic approach to the local scaling relation between SMBH mass galaxy bulge mass. Note that this study uses galaxy stellar mass and galaxy bulge mass interchangeably. Also note that we approximate the local scaling relation slope to be 1 for the sake of simplicity.

more low-mass AGN that are less luminous. Increasing M_{*crit} will result in the opposite behavior: higher mass AGN that are overall more luminous.

Universal Supermassive Black Hole Accretion Model

We incorporate a model for the difference in accretion behavior across the two eras. We do this by enforcing consistency between the average growth rate of galaxies, given observationally, through the star-forming sequence and our relation between stellar mass and SMBH mass. This model should resemble the inconsistent and consistent accretion events in the pre-disk and post-disk eras respectively.

To describe this behavior, we draw from a Gaussian distribution; the distribution has some variance, as a free parameter, and a mean value that we can calculate analytically. For each of the two eras, we assign a unique variance to establish a universal relation to describe SMBH accretion rate ($\dot{\mathrm{M}}_{\mathrm{BH}}$) in that era across all SMBH masses and redshift. This universal relation is defined through the quantity

$$\mathrm{X} \equiv \frac{\dot{\mathrm{M}}_{\mathrm{BH}}}{\langle \dot{\mathrm{M}}_{\mathrm{BH}} \rangle}.$$

The quantity X, by design, has the characteristic $\langle \mathrm{X} \rangle \equiv 1$ and is described by a log-normal distribution. Thus each era will have an established log-normal distribution of accretion rates described exclusively through a unique variance $\sigma_{\ln \mathrm{X}}$. The probability distribution function (PDF) is written as

$$p\left[\ln \mathrm{X}\right] = \frac{1}{\sigma_{\ln \mathrm{X}}\sqrt{2\pi}} \exp\left(\frac{-\left(\ln \mathrm{X} - \mu_{\ln \mathrm{X}}\right)^2}{2\sigma_{\ln \mathrm{X}}^2}\right). \qquad \text{(Eq. 6)}$$

Using the variance $\sigma_{\ln \mathrm{X}}$ and the fact that $\langle \mathrm{X} \rangle \equiv 1$, we constrain the mean value $\mu_{\ln \mathrm{X}}$ using the fact

$$\langle \mathrm{X} \rangle = \exp\left(\mu_{\ln \mathrm{X}} + \frac{\sigma_{\ln \mathrm{X}}^2}{2}\right), \qquad \text{(Eq. 7)}$$

so the analytically determined mean is $\mu_{\ln \mathrm{X}} = -0.5\sigma_{\ln \mathrm{X}}^2$. We expect the spread of accretion rates to be drastically different between pre-disk and post-disk eras, but fairly consistent within an era. The sporadic accretion events of the pre-disk era manifest in this model through a higher variance value. The consistent events of the post-disk era manifest through a variance smaller than that of the pre-disk era.

In order to implement the accretion model we have just set up, we need to relate SMBH mass and galaxy stellar mass to SMBH accretion rate. We begin with the identity

$$\frac{d\mathrm{M}_{\mathrm{BH}}}{dt} = \frac{\mathrm{M}_{\mathrm{BH}}}{\mathrm{M}_*} \frac{d \ln \mathrm{M}_{\mathrm{BH}}}{d \ln \mathrm{M}_*} \frac{d\mathrm{M}_*}{dt}. \qquad \text{(Eq. 8)}$$

We then implement the relations we set up in *Stellar Mass - Supermassive Black Hole Mass*

Relation as

$$\left\langle \dot{\mathrm{M}}_{\mathrm{BH}} \right\rangle = \begin{cases} a\mathrm{M}_{\mathrm{BH}}\frac{\left\langle \dot{\mathrm{M}}_{*} \right\rangle}{\mathrm{M}_{*}} & \mathrm{M}_{*} < \mathrm{M}_{*\mathrm{crit}} \\ \\ \alpha\beta\mathrm{M}_{*}^{\beta-1}\left\langle \dot{\mathrm{M}}_{*} \right\rangle & \mathrm{M}_{*} > \mathrm{M}_{*\mathrm{crit}} \end{cases} \tag{Eq. 9}$$

where the values for α, β, a, and $\mathrm{M}_{*\mathrm{crit}}$ are defined in said section. We get values for specific star formation rate (sSFR or $\dot{\mathrm{M}}_{*}/\mathrm{M}_{*}$) for a given redshift from UM, which we can interpolate for use in our calculations. Eq. 9 provides an average SMBH accretion rate, $\left\langle \dot{\mathrm{M}}_{\mathrm{BH}} \right\rangle$, directly related to M_{*} and z.

We relate luminosities and accretion rates through the following formulations. The Eddington luminosity and accretion rate are given through

$$\mathrm{L}_{\mathrm{Edd}} = \epsilon\dot{\mathrm{M}}_{\mathrm{Edd}}\mathrm{c}^{2} = \frac{\mathrm{M}_{\mathrm{BH}}}{\mathrm{M}_{\odot}}1.26 \times 10^{38}\mathrm{erg/s}\left(\frac{\epsilon}{1.0}\right), \tag{Eq. 10}$$

where ϵ represents the efficiency with which the accreted mass-energy is released as luminosity. We can then calculate a bolometric luminosity, $\mathrm{L}_{\mathrm{bol}}$, and Eddington ratio, η.

$$\mathrm{L}_{\mathrm{bol}} = \epsilon\dot{\mathrm{M}}_{\mathrm{BH}}\mathrm{c}^{2} \tag{Eq. 11}$$

$$\eta \equiv \frac{\dot{\mathrm{M}}_{\mathrm{BH}}}{\dot{\mathrm{M}}_{\mathrm{Edd}}} \tag{Eq. 12}$$

We will assume an efficiency of $\epsilon = 0.1$ (which translates to 10% of the accreted matter being emitted as energy) throughout our calculations. We can implement these relations with the accretion model set up at the start of this section to produce various distributions (e.g. η, $\dot{\mathrm{M}}_{\mathrm{BH}}$, etc.). Figure 2 shows examples of accretion rate and Eddington ratio distributions resulting from our accretion model.

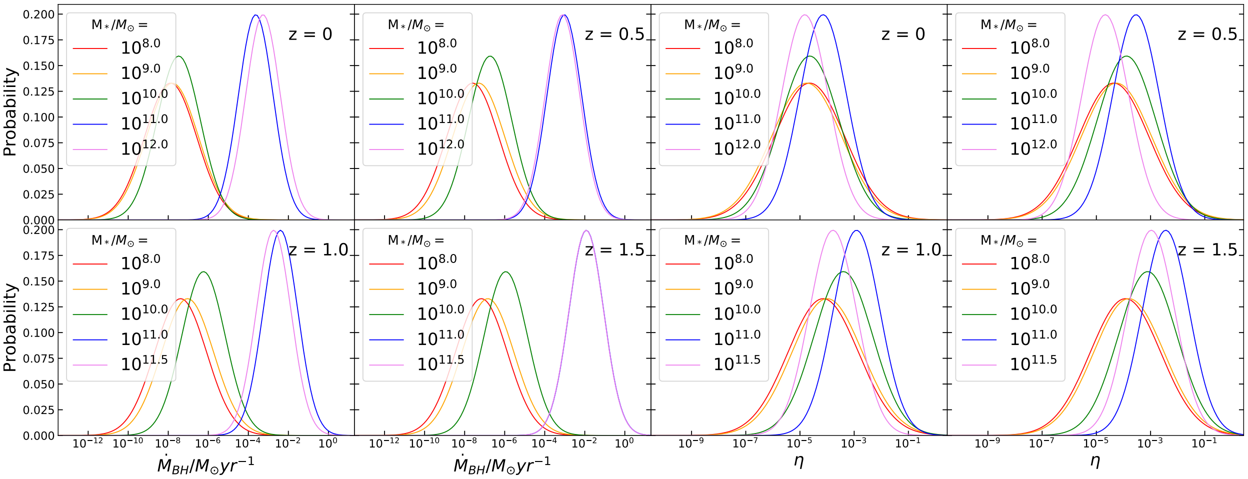

Figure 2: Accretion related distributions generated through the universal accretion model. **Left four panels:** $\dot{\mathrm{M}}_{\mathrm{BH}}$ distributions for varying M_* at different z displayed in units of solar mass per year. The process for which these distributions are calculated is laid out in *Universal Supermassive Black Hole Accretion Model*. **Right four panels:** η distributions for varying M_* at different z. These distributions are calculated almost exactly as the M_* distributions with the small variation of $\dot{\mathrm{M}}_{\mathrm{Edd}}$ where we use Eq. 12 and Eq. 10

Mathematical Pipeline

In this section we discuss the formulations we use to calculate the QLF using relations described in the previous sections. We model scatter consistently throughout our formulations by the use of log-normal probability distribution functions. Throughout this section we use the terminology “direct conversion" which we intend to mean calculating value A from value B by using the relation between A and B without implementing any form of scatter or uncertainty.

Obtaining the Stellar Mass Function

The foundation of all calculations is the HMF which describes the abundance of dark matter halos (and the galaxies contained within) throughout the Universe. We convert the HMF ($\frac{d\mathrm{N}}{d\ln \mathrm{M_H}}$) to a stellar mass function (SMF, $\frac{d\mathrm{N}}{d\ln \mathrm{M}_*}$) by convolving it with the SMHM relation and a given scatter $\sigma_{\ln \mathrm{M}_*}$. The formulation follows from the integral

$$\frac{d\mathrm{N}}{d\ln \mathbf{M}_*} = \int p\left[\ln \mathbf{M}_* | \ln \mathbf{M}_{\mathrm{H}}\right] \frac{d\mathrm{N}}{d\ln \mathbf{M}_{\mathrm{H}}} d\ln \mathbf{M}_{\mathrm{H}}, \qquad \text{(Eq. 13)}$$

with

$$p\left[\ln \mathrm{M}_{*} \middle| \ln \mathrm{M}_{\mathrm{H}}\right] = \frac{1}{\sqrt{2\pi\sigma^{2}_{\ln \mathrm{M}_{*}}}}\exp\left(\frac{-\left(\ln \mathrm{M}_{*} - \mu_{\ln \mathrm{M}_{*}}\right)^{2}}{2\sigma^{2}_{\ln \mathrm{M}_{*}}}\right), \qquad \text{(Eq. 14)}$$

and the dependency $\mathrm{M}_{*}\left(\mathrm{M}_{\mathrm{H}}, z\right)$.

Where $\mu_{\ln \mathrm{M}_{*}}$ is given by the SMHM relation described in *Stellar Mass - Halo Mass Relation* and $\sigma_{\ln \mathrm{M}_{*}}$ is assumed to be 0.7 dex. This PDF describes, for a specific halo mass, the distribution of associated stellar masses. Eq. 13 generates a number density for some value $\ln \mathrm{M}_{*}$ for some redshift, and when we integrate we obtain a component of the SMF. Conducting this calculation for multiple stellar masses gives the total SMF.

Obtaining the Supermassive Black Hole Mass Function

To obtain the SMBH mass function (SMBHMF) we convert the stellar mass function to a black hole mass function using the two-era M_{*}-M_{BH} relation defined in *Stellar Mass - Supermassive Black Hole Mass Relation*. We neglect scatter for this particular conversion because it is already included in the conversion from M_{H} to M_{*} and within the M_{*} to $\dot{\mathrm{M}}_{\mathrm{BH}}$ relation; adding additional scatter here would introduce degeneracy without providing additional physical information.

With no scatter we can retrieve the SMBHMF directly from the SMF and the appropriate slope of the M_{*}-M_{BH} relation in each era defined such that

$$\frac{d\mathrm{N}}{d\ln \mathrm{M}_{\mathrm{BH}}} = \frac{d\mathrm{N}}{d\ln \mathrm{M}_{*}}\frac{d\ln \mathrm{M}_{*}}{d\ln \mathrm{M}_{\mathrm{BH}}}. \qquad \text{(Eq. 15)}$$

This calculation has no explicit dependence on redshift, only implicitly through stellar mass. The step of finding the SMBHMF is unnecessary when considering a no scatter relationship of M_{*}-M_{BH}. This is simply the proof of concept for implementing our various established relationships.

Obtaining the QLF

Convolving the SMF with the relations we defined for M_{*}-M_{BH}, and with Eq. 9 and Eq. 11 we can calculate the bolometric QLF,

$$\frac{d\mathrm{N}}{d\ln \mathrm{L}_{\mathrm{bol}}} = \int p\left[\ln \mathrm{L}_{\mathrm{bol}} \middle| \ln \mathrm{M}_*\right] \frac{d\mathrm{N}}{d\ln \mathrm{M}_*} d\ln \mathrm{M}_*, \qquad \text{(Eq. 16)}$$

with

$$p\left[\ln \mathrm{L}_{\mathrm{bol}} \middle| \ln \mathrm{M}_*\right] = \frac{1}{\sqrt{2\pi\sigma^2_{\ln \dot{\mathrm{M}}_{\mathrm{BH}}}}} \exp\left(\frac{-\left(\ln \dot{\mathrm{M}}_{\mathrm{BH}} - \mu_{\ln \dot{\mathrm{M}}_{\mathrm{BH}}}\right)^2}{2\sigma^2_{\ln \dot{\mathrm{M}}_{\mathrm{BH}}}}\right), \qquad \text{(Eq. 17)}$$

where in our model the bolometric QLF is equivalent to a SMBH accretion rate function due to the functions only differing by a constant (see Eq. 11).

The bolometric luminosity (or SMBH accretion rate) PDF (Eq. 17) is a product of the model described in *Universal Supermassive Black Hole Accretion Model*, with mean and standard deviation

$$\mu_{\ln \dot{\mathrm{M}}_{\mathrm{BH}}} = \mu_{\ln \mathrm{X}} + \ln\left\langle \dot{\mathrm{M}}_{\mathrm{BH}} \right\rangle$$

and

$$\sigma_{\ln \dot{\mathrm{M}}_{\mathrm{BH}}} = \sigma_{\ln \mathrm{X}}$$

respectively.

The formulation for the mean is derived from Eq. 7 and Eq. 9. The standard deviation remains exactly $\sigma_{\ln \mathrm{X}}$ due to the values only differing by a constant. The value for $\ln \dot{\mathrm{M}}_{\mathrm{BH}}$ in the PDF is the direct conversion from $\mathrm{L}_{\mathrm{bol}}$ using Eq. 11. Eq. 17 describes, for a specific quasar bolometric luminosity, a distribution of accretion rates. The last fractional quantity in Eq. 16 represents components of the SMF. An example of our predicted QLF for a representative z value can be seen in 3

To ensure the accretion relation we established follows some form of continuity, we include a smooth linear transition between the pre-disk and post-disk $\sigma_{\ln \mathrm{X}}$ values. This transition expands out from $\mathrm{M}_{*\mathrm{crit}}$ spanning an equal fraction into both the pre-disk era and the "growth" regime of the post-disk era.

This "growth" regime include all bins with an M_* value greater than $\mathrm{M}_{*\mathrm{crit}}$ but also an M_*-

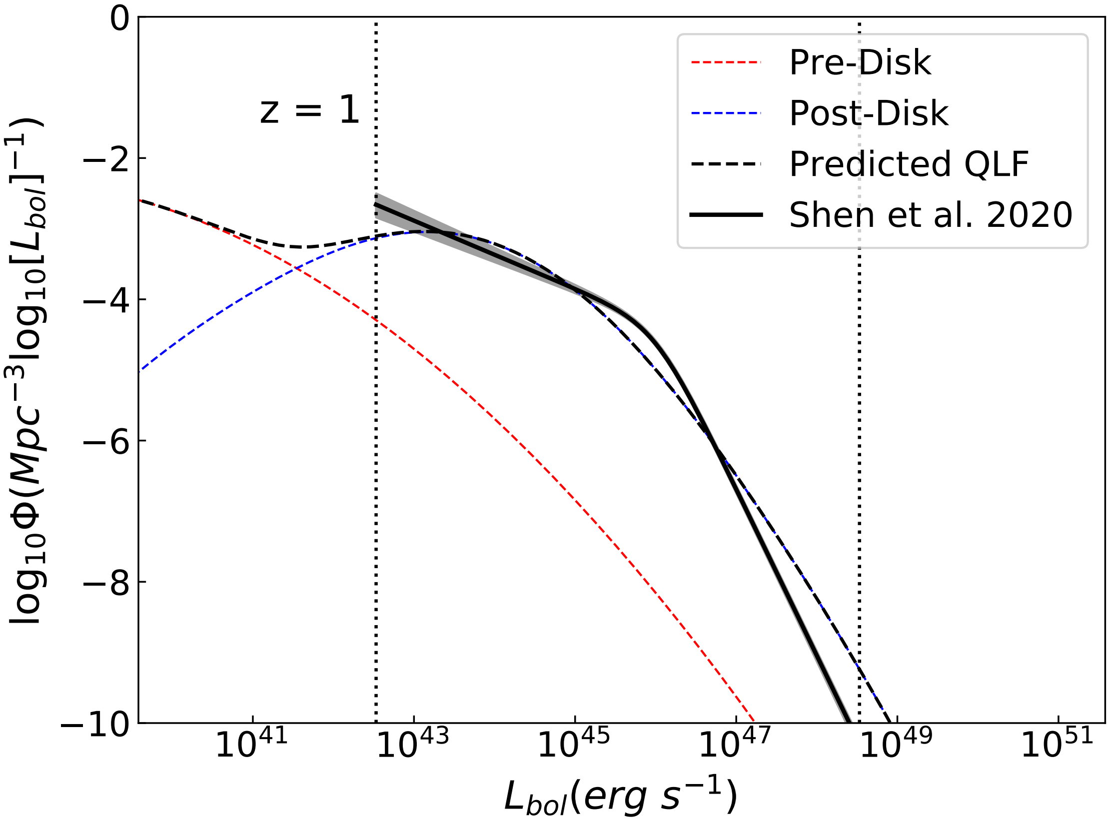

Figure 3: Our predicted QLF with contributions broken down for the pre- and post-disk eras. The black dashed line is our predicted QLF, and solid black line is the QLF best fit to observational data from [15]. Gray scatter correspond to their uncertainty on their best fit parameters to the observational data. The red and blue dashed lines correspond to the pre-disk and post-disk contributions to the predicted QLF respectively.

$\mathrm{M_{BH}}$ slope not within 5% of the local scaling relation (i.e. $\frac{d\ln\mathrm{M_{BH}}}{d\ln\mathrm{M_*}} > 1.05$). The variations in $\sigma_{\ln\mathrm{X}}$ that result from this linear transition can be seen in Figure 2.

Since $\mu_{\ln\mathrm{X}}$ depends on $\sigma_{\ln\mathrm{X}}$, seen in Eq. 7, it also follows the smooth transition across the cut-off. This behavior also influences $\mu_{\ln\dot{\mathrm{M}}_{\mathrm{BH}}}$ due to its dependency on $\mu_{\ln\mathrm{X}}$.

Statistical Extractions

Along with a direct comparison of our QLF model to compiled quasar detection data, we compare aspects of our model to other observational data. The two aspects we explore are SMBH duty cycles ($f\,(\lambda_{\rm sBHAR} > 0.01)$) and specific black hole accretion rates ($\lambda_{\rm sBHAR}$). We utilize data compiled in [16] to make these comparisons. For the two quantities we explore, we explain how [16] define them qualitatively and quantitatively, and how we implement those definitions with our own models.

Specific Black Hole Accretion Rate

This quantity is explained thoroughly in §3.1 and Equation 2 of [16]. We summarize the main points of their definitions needed to make a comparison: $\lambda_{\rm sBHAR}$ is the rate of accretion onto a central SMBH normalized to the host galaxy's stellar mass.

It is defined mathematically as

$$\lambda_{\rm sBHAR} = \frac{k_{\rm bol} L_{\rm X}}{1.3 \times 10^{38} {\rm erg~s^{-1}} \times 0.002 \frac{\rm M_*}{\rm M_\odot}}, \qquad \text{(Eq. 18)}$$

where $k_{\rm bol}$ is a bolometric correction factor and $L_{\rm X}$ is the rest-frame X-ray luminosity of the SMBH. We assume that $k_{\rm bol} L_{\rm X} = L_{bol}$.

They state the scaling factors were chosen so that $\lambda_{\rm sBHAR} \approx \eta$ under the assumption that there is a direct scaling relation between the SMBH and its host galaxy. When you replace $0.002\frac{\rm M_*}{\rm M_\odot}$ with $\rm M_{BH}$, Eq. 18 is exactly the Eddington ratio.

The main difference of our model is that it explores a scaling relation that is *not* direct, so we compare our model to the [16] data using two different methods: (1) We will assume $\lambda_{\rm sBHAR} = \eta$ and use the η distributions of our model (see Figure 2) as $\lambda_{\rm sBHAR}$ when comparing to their data. (2) We use their definition exactly by using $\dot{\rm M}_{\rm BH}$ distributions of our model (see Figure 2) along with Eq. 11 to calculate $L_{\rm bol}$. We then use this value in Eq. 18.

We believe method (2) will provide the best possible comparison as it most closely resembles their methods; their study's values are not directly Eddington ratios, but are a result of post-processed observational data. We conduct the process for method (1) to explore discrepancies.

Duty Cycle

In [16], they define the duty cycle in §3.4 as the fraction of central SMBHs that are accreting above the limit $\lambda_{\mathrm{sBHAR}} = 0.01$. The fractional duty cycle of a given stellar mass at a given redshift (fraction of SMBH with $\lambda_{\mathrm{sBHAR}} > 0.01$) is defined as $f(\lambda_{\mathrm{sBHAR}} > 0.01)$ in Equation 3 of [16].

We extrapolate their equation to fit our model in two steps. First we define a duty cycle for a singular M_* and redshift,

$$f(\lambda_{\mathrm{sBHAR}} > 0.01, \mathbf{M}_*, z) = \int_{-4.6}^{\infty} p\left(\ln \lambda_{\mathrm{sBHAR}} | \ln \mathbf{M}_*, z\right) d \ln \lambda_{\mathrm{sBHAR}}, \qquad \text{(Eq. 19)}$$

where $p\left(\ln \lambda_{\mathrm{sBHAR}} | \ln \mathbf{M}_*, z\right)$ is the probability distribution of λ_{sBHAR} calculated as explained in *Specific Black Hole Accretion Rate* by use of methods (1) and/or (2) and $-4.6 \approx \log\left[0.01\right]$.

When plotting the fractional duty cycle, the data was binned into different stellar mass ranges. So, second we consider the stellar mass weights that are naturally seen in observational data by implementing the SMF into the calculation with our model's data. To do this we integrate the duty cycle over the stellar mass range using the SMF as a weight, seen by

$$f(\lambda_{\mathrm{sBHAR}} > 0.01) = \frac{\int_{\mathrm{M}_*^1}^{\mathrm{M}_*^2} f\left(\ln \lambda_{\mathrm{sBHAR}} | \ln \mathbf{M}_*, z\right) \frac{d\mathrm{N}}{d \ln \mathrm{M}_*} d \ln \mathbf{M}_*}{\int_{\mathrm{M}_*^1}^{\mathrm{M}_*^2} \frac{d\mathrm{N}}{d \ln \mathrm{M}_*} d \ln \mathbf{M}_*}, \qquad \text{(Eq. 20)}$$

where M_*^1 and M_*^2 corresponds to the edges of the stellar mass bin we plot the fractional duty cycle for. The duty cycle for methods (1) and (2) can be seen in the left panels of Figures 4 and 5 respectively.

Average Specific Black Hole Accretion Rate

The average λ_{sBHAR} of AGN ($\langle\lambda_{\mathrm{sBHAR}}\rangle$) is defined in [16] §3.4 as the average λ_{sBHAR} for galaxies with SMBH accretion at a rate $\lambda_{\mathrm{sBHAR}} > 0.01$. We calculate this value from our model similarly to how we did for the duty cycle. Modifying Equation 4 in [16] we get our formulation as

$$\left\langle \lambda_{\mathrm{sBHAR}} \right\rangle (\mathbf{M}_*, z) = \int_{-4.6}^{\infty} p\left(\ln \lambda_{\mathrm{sBHAR}} | \ln \mathbf{M}_*, z\right) \lambda_{\mathrm{sBHAR}} d \ln \lambda_{\mathrm{sBHAR}}, \qquad \text{(Eq. 21)}$$

which fits into

$$< \lambda_{\mathrm{sBHAR}} >= \frac{1}{f(\lambda_{\mathrm{sBHAR}} > 0.01)} \times \frac{\int_{\mathrm{M}_*^1}^{\mathrm{M}_*^2} < \lambda_{\mathrm{sBHAR}} > (\mathbf{M}_*, z) \, \frac{dN}{d \ln \mathrm{M}_*} d \ln \mathbf{M}_*}{\int_{\mathrm{M}_*^1}^{\mathrm{M}_*^2} \frac{dN}{d \ln \mathrm{M}_*} d \ln \mathbf{M}_*}. \qquad \text{(Eq. 22)}$$

The value $\langle \lambda_{\mathrm{sBHAR}} \rangle$ for methods (1) and (2) can be seen in the right panels of Figures 4 and 5 respectively.

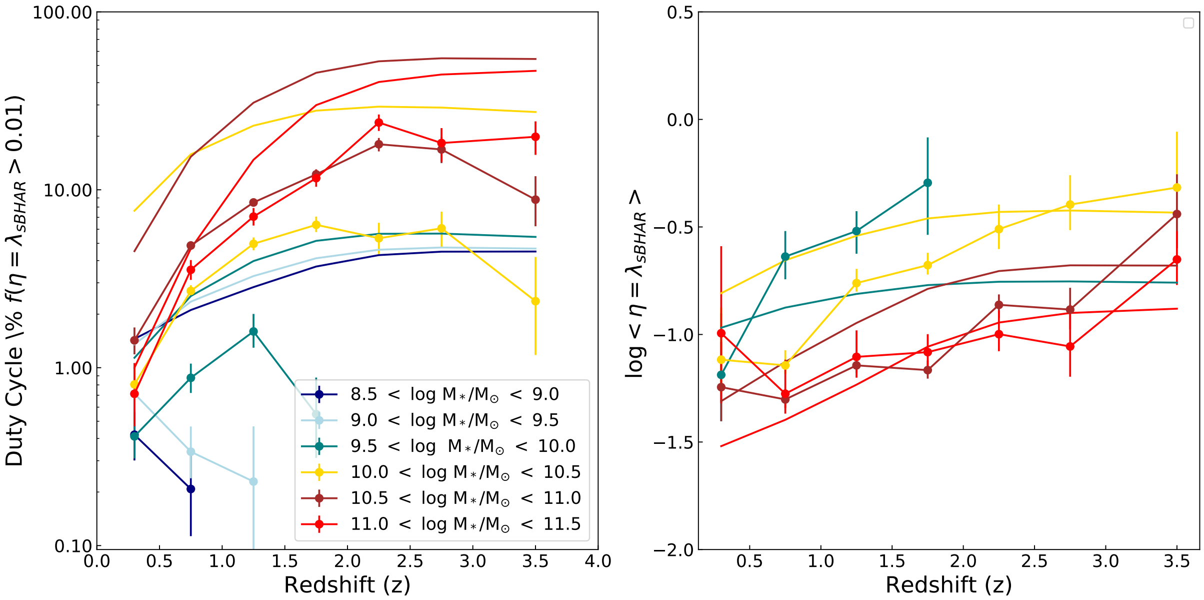

Figure 4: **Left panel:** $f(\lambda_{\rm sBHAR} > 0.01)$ as described in *Duty Cycle*. **Right panel:** $\langle\lambda_{\rm sBHAR}\rangle$ as described in *Average Specific Black Hole Accretion Rate*. The lower mass bins are not displayed in this panel as there was significant uncertainty in the observational data (see [16] for additional details). In both panels, the dotted points with error bars represent data from [16], and the smooth lines represent the predictions of our model. The different colored lines correspond to different mass bins and are labeled in a legend that applies to both panels. In this figure, we calculated the quantities from our model using the assumption $\lambda_{\rm sBHAR} = \eta$ (method (1) in *Specific Black Hole Accretion Rate*).

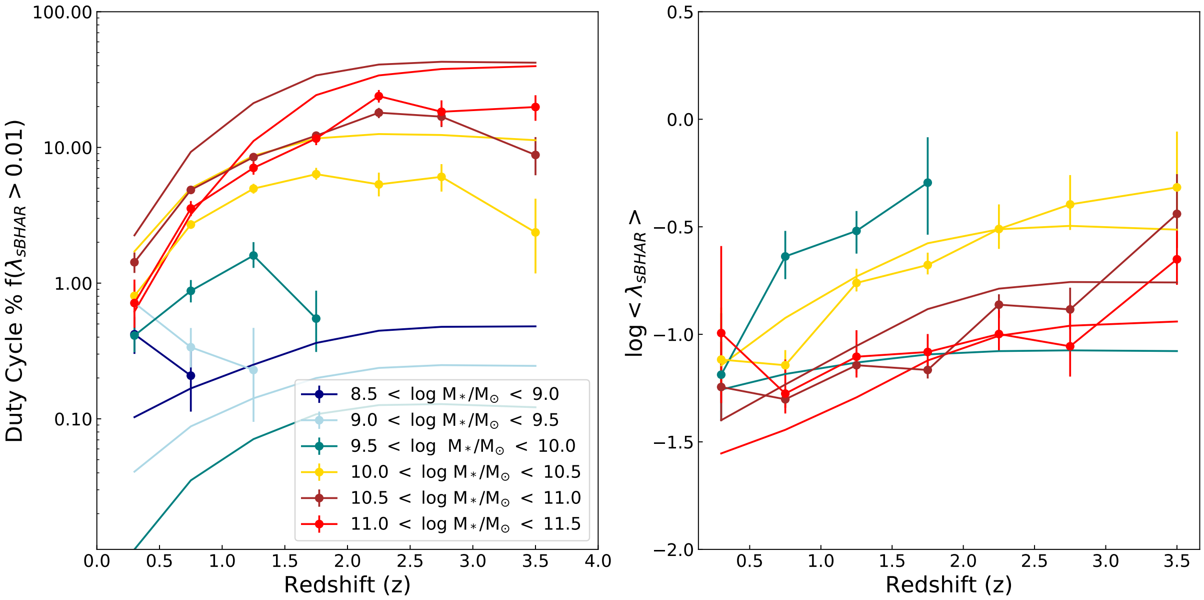

Figure 5: Same as Figure 4 but using method (2) as described in *Specific Black Hole Accretion Rate*.

SECTION III

RESULTS

The Predicted QLF

The shape of our predicted QLF, seen in Figures 3 and 6, is defined by two distinct peaks; one at an un-observable low luminosity and one within the observable luminosity range. As seen in these Figures, the peak at low luminosity is dominated by quasars populating the pre-disk era. The higher luminosity peak is dominated by quasars of the post-disk era.

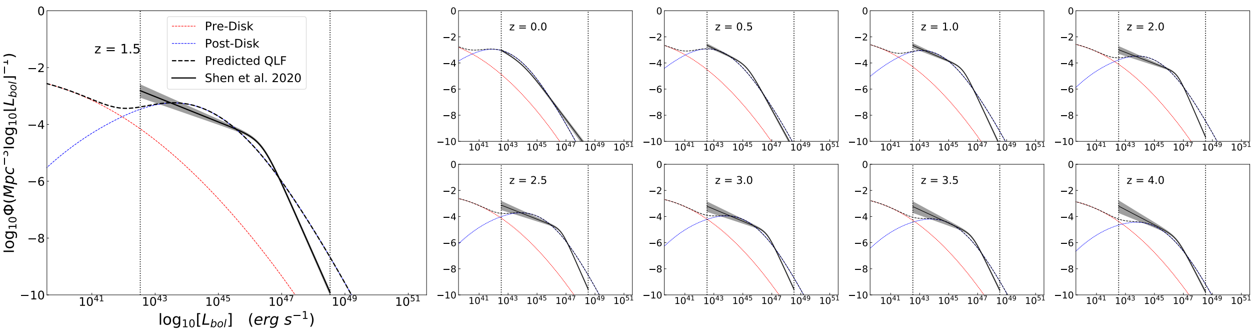

Figure 6: Same as Figure 3 but for various redshift values ranging from 0 to 4. The axes on the smaller plots are identical to those on the largest plot.

When analyzing our predicted QLF, we compare to observational data compiled in [15], which is an update on the [17] study. Within their study, they produce constraints on the bolometric QLF from $z = 0$ to $z = 7$. They analyze multi-band observational data to do so. The limitations of this comparison comes from the lack of observational data at the low luminosity end which is also where our model differs from most others.

Our predicted QLF shape differs from typical QLF models which tend to express a “knee” fit function (e.g. the single turnover or change in slope which can be seen in the [15] fits). Instead, in our prediction, we see a valley produced at the low luminosity end due to the gap between each eras' contribution to the overall QLF. This gap is due to the nature of the universal accretion rate model our study implements. Our model produces accretion property distributions that differ for various M_* values and between the pre-disk and post-disk eras.

The gap is partially a result of the $\sigma_{\ln X}$ parameters we implement, and the gap would narrow slightly if the two $\sigma_{\ln X}$ values were chosen to be closer in quantity. If we had chosen one representative accretion distribution our predicted shape would more resemble that of many other studies. The "knee" shape most studies see results from a constant Eddington ratio distribution which produces that single turnover function. Again, since the differences in shapes occurs at the un-observable end of the QLF, direct exploration is limited. We will explore this problem again later on.

Looking at the observable end of the QLF, our predictions agrees fairly well with observational data. Some z values match much better than others. For example, looking at Figure 6, our predicted QLF from $z = 1.5$ to $z = 2.5$ struggles to match the observable data more than other z values.

It is important to note that the observational data at higher z values becomes more scarce and that lower luminosity AGN are harder to detect. These observational biases are not something we directly take into account when producing our predictions and thus reveals another limitation in this direct comparison to observed QLF data.

The [15] study finds that the low luminosity end of their fits become progressively steeper at higher redshifts. We also see this behavior in our predictions; higher redshift values shift the contribution balance away from the post-disk era and towards the pre-disk era. This produces a larger peak to peak difference between those contributions thus increasing the slope of the QLF at the low luminosity end.

We explore the best fit parameters of our QLF model to this observational data later in the section.

The Duty Cycle and Average Specific Black Hole Accretion Rate

In **Statistical Extractions** we discussed how to further explore our model's predictions through $f\left(\lambda_{\text{sBHAR}} > 0.01\right)$ and $\langle\lambda_{\text{sBHAR}}\rangle$. We did this utilizing two methods (1) assuming $\lambda_{\text{sBHAR}} = \eta$ and (2) using their exact definition for λ_{sBHAR}. The results of these methods can be seen in Figures 4 and 5 respectively. We first discuss possible trends in the [16] data we compare to, then discuss the co-existence or lack there of these trend in our predictions. Note that the uncertainty associated with the observational data is quite large for some points and the trends we claim to see are considered within these uncertainties.

On the Duty Cycle

For the duty cycle (left panels of Figures 4 and 5) we point out two behaviors of the [16] data: (i) Looking at the mass bins collectively, there tends to be higher $f\left(\lambda_{\text{sBHAR}} > 0.01\right)$ for larger M_*. Of the highest two mass bins, each are about half above and half below the other. This could imply that one bin is actually completely above or below the other, or simply that they do overlap at some points. Considering the uncertainty on the data, each scenario is equally likely. (ii) Each mass bin's $f\left(\lambda_{\text{sBHAR}} > 0.01\right)$ tends to increase with increasing redshift up to a point, after which we see a decrease. This does not hold for the lowest mass bins, but the study claims the lowest masses likely have larger uncertainties associated.

Looking at method (1) of our model's predictions, behavior (i) holds up for the most part for all mass bins. Behavior (ii) also holds up except instead of a decrease, our predictions tend to plateau as z increases. We also see that all of the mass bins in our predictions tend to exhibit a higher $f\left(\lambda_{\text{sBHAR}} > 0.01\right)$ than the [16] data.

Looking at method (2) of our model's predictions, behavior (i) does not hold well apart from the lowest mass bins having smaller $f\left(\lambda_{\text{sBHAR}} > 0.01\right)$ than the highest mass bins. We also see some overlapping in the highest mass bins' values at higher redshifts which resembles the overlap seen in the observational data. Behavior (ii) holds in the same way as it did for method (1). We also see that for the lowest three mass bins, our predictions show much lower $f\left(\lambda_{\text{sBHAR}} > 0.01\right)$ than what the [16] data exhibits, but the highest mass bins match better than they did for method

(1).

On the Average Specific Black Hole Accretion Rate

For the average $\lambda_{\rm sBHAR}$ (right panels of Figures 4 and 5) we point out two behaviors of the [16] data: (i) Opposite to what $f\,(\lambda_{\rm sBHAR} > 0.01)$ showed, $\langle\lambda_{\rm sBHAR}\rangle$ tends to decrease with higher mass bins. We again see an overlapping of the highest two mass bins. (ii) Each mass bin's $\langle\lambda_{\rm sBHAR}\rangle$ tends to increase with increasing redshift, apart from a few points. Also note that the $\langle\lambda_{\rm sBHAR}\rangle$ values tend to have much larger relative uncertainty than the fractional duty cycle.

Looking at method (1) of our model's predictions, behavior (i) holds apart from the lowest mass bin which overlaps with the higher mass bins and tends to under-predict the observational data. Behavior (ii) holds but again exhibiting the plateau at higher redshift. However, the plateau behavior seems to match the observational data better for $f\,(\lambda_{\rm sBHAR} > 0.01)$ than for $\langle\lambda_{\rm sBHAR}\rangle$.

Looking at method (2) of our model's predictions, both behaviors (i) and (ii) hold in similar ways as they did for method (1). Though it could be said that the second to lowest mass bin matches the observational data better than it did for method (1), and the lowest mass bin under-predicts the observational data more than method (1). It seems our predictions for $\langle\lambda_{\rm sBHAR}\rangle$ vary little between methods (1) and (2). The major differences in the methods appears in $f\,(\lambda_{\rm sBHAR} > 0.01)$ and mainly in the lowest mass bins.

Which method provides an objectively better comparison to observable data is hard to say. In our study, we favor method (2) as it most closely resembles how the [16] study processed their data. We explore the best fit parameters of our QLF model by fitting method (2) to this observational data. We discuss this process in the following sub-section.

Best Fit Parameters

We have three free parameters in our QLF model (pre-disk $\sigma_{\ln \rm X}$, post-disk $\sigma_{\ln \rm X}$, and $\rm M_{*crit}$) that we want to constrain using the observational data. Doing this will allow us to make more confident conclusions on the results of this study. We find our best fit parameters by calculating the least squares value for a 3-dimensional parameter space. We limit the parameter space to contain only physically reasonable sets of values for each of our three free parameters.

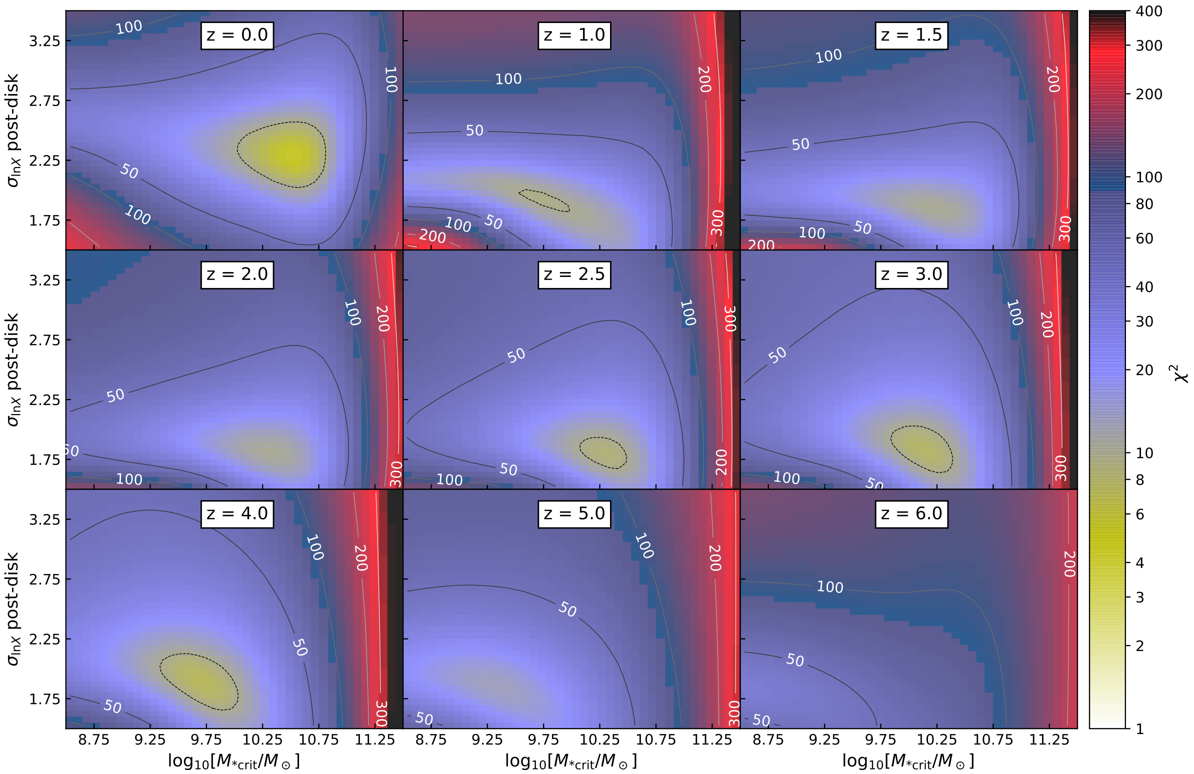

Figure 7: Likelihood of best fit grids to the [15] data for the free parameters $M_{*\rm crit}$ and post-disk $\sigma_{\ln X}$ at various redshifts. These are plotted assuming the third parameter, pre-disk $\sigma_{\ln X}$, is optimized. The dashed black lines corresponds to a contour of $\chi^2 = 10$. The color-bar applies to all grids and displays χ^2 or the goodness of fit. Values closer to zero correspond to a better fit to the data.

The first fit we produce is comparing our predicted bolometric QLF to the compiled observational data in the [15] study. Their study includes uncertainties on their best fit parameters, which propagates to their QLF fit curves and can be seen in Figures 3 and 6 as the gray area around said curves. We choose to ignore these uncertainties when running our script since we are comparing to a fit to observational data and not directly to the observational data itself.

We only fit the bolometric QLF between the luminosity range of $10^{8.95}$ to $10^{14.95} \mathrm{L_{bol}/L_\odot}$ since that is where the majority of the [15] observational data was available. The result of this fit can be seen in Figure 7. We find a fairly consistent set of best fit parameters across different

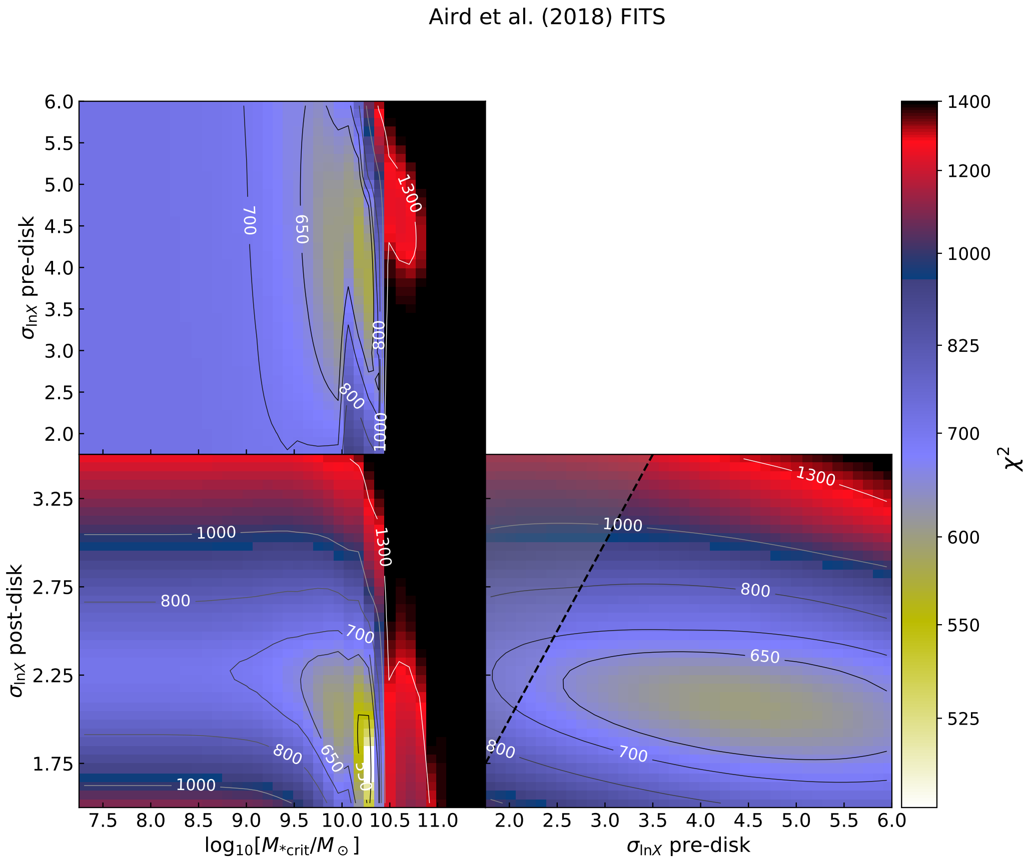

Figure 8: Likelihood of best fit grids for all three free parameters to the [16] data. In each 2-dimensional plot the third parameter is optimized. The dashed line corresponds to pre-disk $\sigma_{\ln \mathrm{X}}$ = post-disk $\sigma_{\ln \mathrm{X}}$. The values above the line are not expected to be physically reasonable for our model.

redshift values. The fits become less consistent starting at $z = 5$ but the observational data available at higher redshift is scarce. We only display the parameter space of two parameters, post-disk $\sigma_{\ln \mathrm{X}}$ and $\mathrm{M}_{*\mathrm{crit}}$, since the third parameter, pre-disk $\sigma_{\ln \mathrm{X}}$ is very poorly constrained by the [15] data. These 2-dimensional parameter spaces are displayed assuming that the 3rd parameter is optimized.

The second fit we produce is comparing the observational data of [16], $f\left(\lambda_{\mathrm{sBHAR}} > 0.01\right)$ and $\langle\lambda_{\mathrm{sBHAR}}\rangle$, to predictions produced using our models and relations. When running our script, we fit $f\left(\lambda_{\mathrm{sBHAR}} > 0.01\right)$ and $\langle\lambda_{\mathrm{sBHAR}}\rangle$ simultaneously. We do this both across all redshift values (see Figure 8), and for each redshift individually (see Figure 9).

We weigh our fit using the error bars provided by the [16] study. These are implemented in the denominator of the least squares sum, and we cap the ratio of the prediction vs. observation difference squared over the error squared at 100. This ensures that our fits will not fixate on the points with the smallest errors since the errors vary so drastically.

In Figure 8, we display all three 2-dimensional parameter spaces in a corner layout, each space assuming the 3rd unseen parameter is optimized. We find that the best fit values for $\mathrm{M}_{*\mathrm{crit}}$ and post-disk $\sigma_{\ln \mathrm{X}}$ align with what we saw in our predicted QLF fits. Unlike the QLF fits, the pre-disk $\sigma_{\ln \mathrm{X}}$ is constrained better allowing us to confidently pick all three optimized parameters for our study.

We find that there is not a significant trend with redshift when fitting each redshift value independently instead of together (see Figure 9). The amount of data available to fit is already limited when considering every redshift value and becomes even more limited for individual redshifts. Therefore, running fits based on individual redshifts is not likely to give us a confident constraint on our model's free parameters.

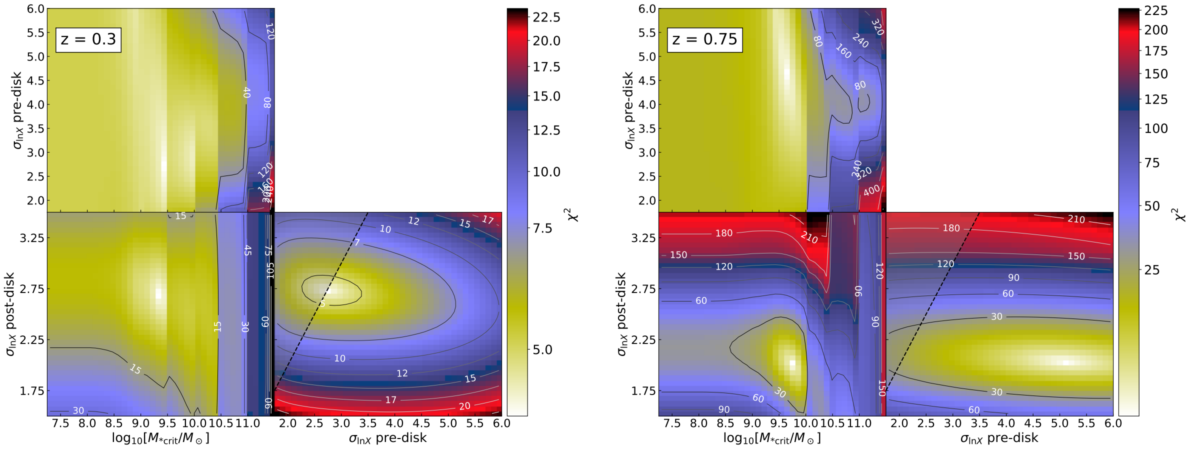

(a) z = 0.3 (b) z = 0.75

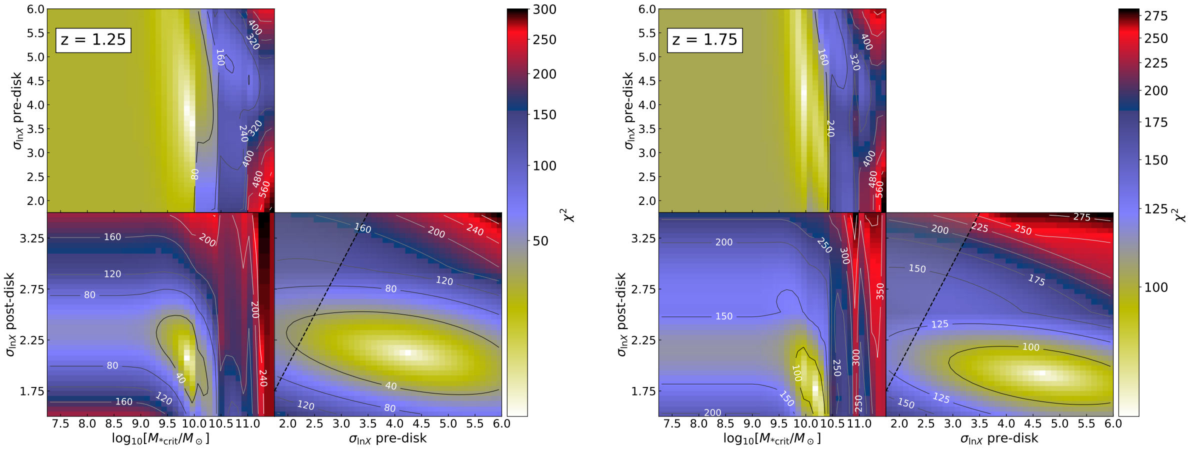

(c) z = 1.25 (d) z = 1.75

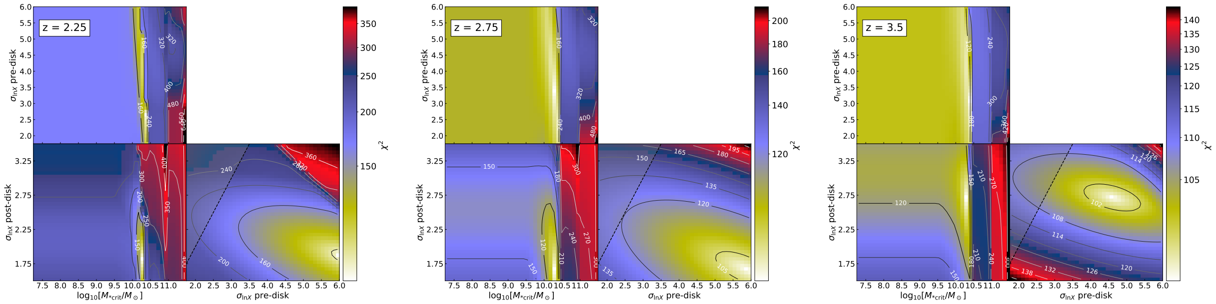

(e) z = 2.25 (f) z = 2.75 (g) z = 3.5

Figure 9: Same as Figure 8 but for the individual redshift values z = 0.3, 0.75, 1.25, 1.75, 2.25, 2.75, and 3.5. All axes are identical but the color scale varies between plots.

SECTION IV

DISCUSSION

The Free Parameters

The effects of varying our model's three free parameters on the overall shape of the QLF can be seen in Figure 10 and are discussed as follows.

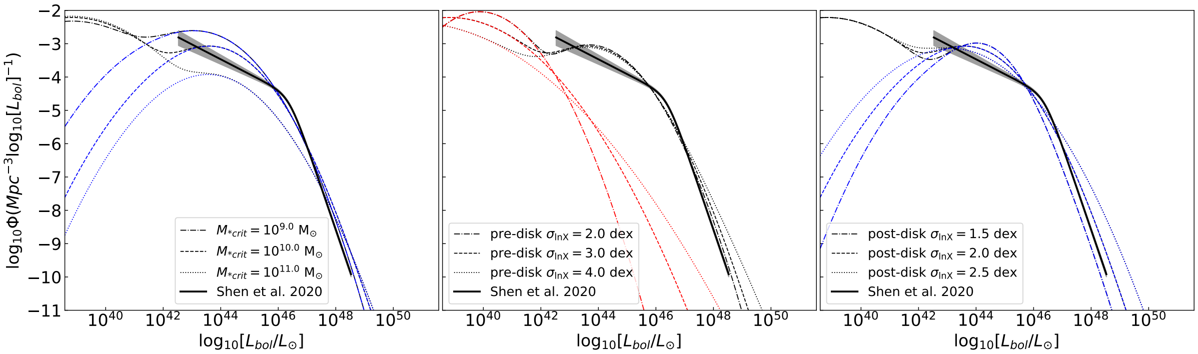

Figure 10: Effects of varying the three free parameters of our model on the predicted QLF. Non-solid black lines correspond to the total predicted QLF. Red lines correspond to the pre-disk contribution to the predicted QLF. Blue lines correspond to the post-disk contribution. The solid black line corresponds to the observational fit of [15]. The left, middle, and right sub-plots correspond to variances in the $M_{*\mathrm{crit}}$, pre-disk $\sigma_{\ln X}$, and post-disk $\sigma_{\ln X}$ parameters respectively. In each sub-plot, if an era is not affected by varying the free parameter displayed then its contribution is not plotted.

Pre-disk $\sigma_{\ln X}$ Parameter

This parameter only affects the pre-disk contribution to the predicted QLF noticeably. Changes in this value only affects the very low and very high luminosity (less so) ends of the QLF. By increasing the value we see a decrease in quasar density at lower un-observable luminosities and an increase in quasar density at higher luminosities where observational data is available.

Overall this parameter does not significantly affect the shape of our predicted QLF thus we find it reasonable to accept the best fit value of ≈ 3.75 dex. This value is well within the fit constraint that the [16] data gave through our least squares calculations. This value being fairly high also confirms the idea that the pre-disk accretion events are scattered and inconsistent.

Post-disk $\sigma_{\ln \mathrm{X}}$ *Parameter*

This parameter only affects the post-disk era. An increase in this value sees an increase in density at the high luminosity end of the QLF. The increased scatter also sees a corresponding decrease in the mean values for luminosity (recall the dependency of $\mu_{\ln \mathrm{X}}$ on $\sigma_{\ln \mathrm{X}}$). This change in mean values follows directly from the way we set-up the SMBH accretion model (see *Universal Supermassive Black Hole Accretion Model*).

Based on both of the observational fits we ran, we find the best fit value for this parameter to be ≈ 2.0 dex. This value is lower than the pre-disk value which is the relation we expected to see to confirm the accretion behaviors we saw in the simulations. The smaller value implies that the accretion events in the post-disk era are much more consistent than those in the pre-disk era.

The $\mathrm{M}_{*\mathrm{crit}}$ *Parameter*

This parameter affected the post-disk era growth regime in the most noticeable way. It is also the parameter that has the largest effect on the overall shape of the predicted QLF.

When a low mass value is chosen for $\mathrm{M}_{*\mathrm{crit}}$, we see a dramatic increase in lower luminosity quasar density. In this case the contributions come from mainly lower mass SMBHs which end up corresponding to lower luminosity quasars (see Figure 1). When a larger mass value for $\mathrm{M}_{*\mathrm{crit}}$ is chosen, a much larger range of SMBH masses contribute, from which the more massive SMBHs will produce more luminous quasars increasing the high luminosity density of the predicted QLF.

For this parameter, a value close to $\mathrm{M}_{*\mathrm{crit}} = 10^{10}$ or $10^{11}\mathrm{M}_*/\mathrm{M}_\odot$ would resemble the delayed growth behavior this study aimed to explore. We find that our fits support a best fit value of $\mathrm{M}_{*\mathrm{crit}} \approx 10^{10.25}\mathrm{M}_*/\mathrm{M}_\odot$ thus the delayed growth behavior appears to be favored.

On the Lack of Low Luminosity Quasar Detection

The overall shape of our predicted QLF varies enough from the “knee” fit function (typically produced by QLF models assuming continuous BH growth) to provoke a consideration on the extent to which our best fit values are valid. Fitting our predicted QLF to those from [15] proves difficult since our predictions exhibit a double turnover behavior while theirs exhibit a single turnover. This typically proves hardest to match at the knee of their QLF and at the high luminosity end of the QLF.

We address a possible bias in our consideration on what constitutes a valid pre-disk $\sigma_{\ln \mathrm{X}}$ value. We have little observational data to motivate a fit at the low luminosity end of the QLF where the pre-disk portion contributes. Our QLF fits (Figure 7) display the other two free parameters with the third (pre-disk $\sigma_{\ln \mathrm{X}}$) optimized. These optimized values imply a best-fit value of pre-disk $\sigma_{\ln \mathrm{X}} \approx$ 3-4 dex. But these values are not heavily favored, and if the actual value is dramatically higher, then the high luminosity end of the QLF will be affect. If this is the case, the other free parameters will need to be adjusted in order compensate for the dramatic change to the predicted QLF. Changing all the best fit parameters in this way could potentially change the results of this study.

We ran fits to $f\left(\lambda_{\mathrm{sBHAR}} > 0.01\right)$ and $\langle\lambda_{\mathrm{sBHAR}}\rangle$ to provide a potential resolution to this issue. We find that again, $\mathrm{M}_{*\mathrm{crit}}$ and post-disk $\sigma_{\ln \mathrm{X}}$ and the most constrained, but pre-disk $\sigma_{\ln \mathrm{X}}$ is constrained better than it was by the QLF fits. This is likely due to the fact that pre-disk $\sigma_{\ln \mathrm{X}}$ affects mostly lower luminosity AGN, thus lower mass BHs, and finally lower galaxy stellar masses. A decent portion of the [16] observational data was for lower stellar masses which allowed a more reliable test for an optimized pre-disk $\sigma_{\ln \mathrm{X}}$ value.

The QLF fits demonstrated a preferred range of values for $\mathrm{M}_{*\mathrm{crit}}$ with smooth transitions to the values surrounding, but the $f\left(\lambda_{\mathrm{sBHAR}} > 0.01\right)$ and $\langle\lambda_{\mathrm{sBHAR}}\rangle$ fits demonstrated a hard cut off at higher values (Figure 8). Looking back at Figure 5 it is clear why this is the case. The highest mass bins have much larger fractional duty cycles than the lowest masses. The stellar mass bin containing the value of $\mathrm{M}_{*\mathrm{crit}}$ sits directly between the highest and lowest duty cycles.

Our model is set up to produce high mass, high luminosity AGN beginning after the transition to the post-disk era marked by $\mathrm{M}_{*\mathrm{crit}}$. The definition for the duty cycle we have set up considers only higher luminosity AGN as quasars thus the duty cycle for M_{*} values after $\mathrm{M}_{*\mathrm{crit}}$

will be much higher than for those before it. Once you begin to raise $\mathrm{M}_{*\mathrm{crit}}$ past a stellar mass of about $10^{10.5}\mathrm{M}_*/\mathrm{M}_\odot$, then higher stellar masses produce far less high luminosity AGN that can be classified as quasars. This would drop those highest mass bins, in the left panel of Figure 5, down to similar values that the lowest mass bins have; this would then produce a far worse fit. Thus the preference for larger $\mathrm{M}_{*\mathrm{crit}}$ values drops quickly.

SECTION V

CONCLUSION

The predicted QLF from our model is based on both observational data and theoretical behaviors seen in the FIRE simulations. Running fit techniques on our predictions with various observational data allowed us to quantify the allowed scenarios in which our predicted QLF is valid. We found fairly well constraints on our best fit parameters that support the behaviors we aimed to explore.

We found that the best fit values for the pre- and post-disk era $\sigma_{\ln \mathrm{X}}$ parameters supports the accretion behavior the simulations exhibit. The SMBH grows slowly through inconsistent accretion events at first, which is supported by a large $\sigma_{\ln \mathrm{X}}$ in the pre-disk era. Then coherent fueling allows the SMBH to grow rapidly and consistently, which is supported by a small $\sigma_{\ln \mathrm{X}}$ in the post-disk era. While small and large are relative terms, the main point is that pre-disk $\sigma_{\ln \mathrm{X}} >$ post-disk $\sigma_{\ln \mathrm{X}}$ resembling the difference in accretion event consistency we see in the simulations.

We also found that the allowed best fit values for $\mathrm{M}_{*\mathrm{crit}}$ match what was seen in [10]. This supports the delayed SMBH growth model seen consistently in galaxy formation simulations. The best fit values here line up with this SMBH growth behavior despite this study using galaxy stellar mass and bulge mass interchangeably. Also, the delayed growth best fit value for $\mathrm{M}_{*\mathrm{crit}}$ is not only supported by our fit results, but tends to be favored over the purely linear M_*-M_{BH} growth (which would be represented by a $\mathrm{M}_{*\mathrm{crit}} \approx 10^{8.0}\mathrm{M}_\odot$ or less). These conclusions hold for the redshift values of $z = 0$ to $z = 4$ that we aimed to explore.

Not only did our model predict a QLF that matches observational data fairly well, but it also produced predictions for a duty cycle and specific black hole accretion rate that match observational data. Limitations in matching those quantities lies in the observational uncertainty associated with lower stellar mass galaxy detection and high redshift detection. The observational data we compared to only spans redshift values of $z = 0$ to $z = 4.0$. Despite the limitations, our predictions decently match the observed data both quantitatively and qualitatively.

Implementing an additional sub-model relating galaxy stellar mass to galaxy bulge mass would be insightful since using them interchangeably is typically only valid for bulge dominated galaxies. However observational data relating these quantities seems fairly sparse. Returning to this issue with the desired observational data in the future might be beneficial to confirm the results of this study further.

It appears that both our model and other typical “knee” fit models for the QLF produce allowed scenarios for the emergence of the local observed scaling relation between SMBH mass and galaxy bulge mass. However, this is only considering the limited observational data we have available, and the main differences between these models seems to appear in the low luminosity end of the QLF where little to no observational data is available. We also must acknowledge the difficulty of comparing any model at redshift values higher than z ≈ 4; after this z we struggle due to the sparseness of the observational data. Further observations which push the known QLF down to lower luminosities and/or higher redshifts may be able to distinguish between our delayed BH growth model and models where BHs grow continuously throughout cosmic time.

REFERENCES

[1] M. Vogelsberger, S. Genel, V. Springel, P. Torrey, D. Sijacki, D. Xu, G. Snyder, D. Nelson, and L. Hernquist, “Introducing the Illustris Project: simulating the coevolution of dark and visible matter in the Universe,” , vol. 444, pp. 1518–1547, Oct 2014.

[2] J. Schaye, R. A. Crain, R. G. Bower, M. Furlong, M. Schaller, T. Theuns, C. Dalla Vecchia, C. S. Frenk, I. G. McCarthy, J. C. Helly, A. Jenkins, Y. M. Rosas-Guevara, S. D. M. White, M. Baes, C. M. Booth, P. Camps, J. F. Navarro, Y. Qu, A. Rahmati, T. Sawala, P. A. Thomas, and J. Trayford, “The EAGLE project: simulating the evolution and assembly of galaxies and their environments,” , vol. 446, pp. 521–554, Jan 2015.

[3] R. Teyssier, “Cosmological hydrodynamics with adaptive mesh refinement. A new high resolution code called RAMSES,” , vol. 385, pp. 337–364, Apr 2002.

[4] P. F. Hopkins, D. Kereš, J. Oñorbe, C.-A. Faucher-Giguère, E. Quataert, N. Murray, and J. S. Bullock, “Galaxies on FIRE (Feedback In Realistic Environments): stellar feedback explains cosmologically inefficient star formation,” , vol. 445, pp. 581–603, Nov 2014.

[5] P. F. Hopkins, A. Wetzel, D. Kereš, C.-A. Faucher-Giguère, E. Quataert, M. Boylan-Kolchin, N. Murray, C. C. Hayward, S. Garrison-Kimmel, C. Hummels, R. Feldmann, P. Torrey, X. Ma, D. Anglés-Alcázar, K.-Y. Su, M. Orr, D. Schmitz, I. Escala, R. Sanderson, M. Y. Grudić, Z. Hafen, J.-H. Kim, A. Fitts, J. S. Bullock, C. Wheeler, T. K. Chan, O. D. Elbert, and D. Narayanan, “FIRE-2 simulations: physics versus numerics in galaxy formation,” , vol. 480, pp. 800–863, Oct 2018.

[6] J. Kormendy and L. C. Ho, “Coevolution (Or Not) of Supermassive Black Holes and Host Galaxies,” , vol. 51, pp. 511–653, Aug. 2013.

[7] N. Häring and H.-W. Rix, “On the Black Hole Mass-Bulge Mass Relation,” , vol. 604, pp. L89–L92, Apr 2004.

[8] A. Marconi and L. K. Hunt, “The Relation between Black Hole Mass, Bulge Mass, and Near-Infrared Luminosity,” , vol. 589, pp. L21–L24, May 2003.

[9] D. Anglés-Alcázar, R. Davé, C.-A. Faucher-Giguère, F. Özel, and P. F. Hopkins, “Gravitational torque-driven black hole growth and feedback in cosmological simulations,” , vol. 464, pp. 2840–2853, Jan 2017.

[10] D. Anglés-Alcázar, C.-A. Faucher-Giguère, E. Quataert, P. F. Hopkins, R. Feldmann, P. Torrey, A. Wetzel, and D. Kereš, “Black holes on FIRE: stellar feedback limits early feeding of galactic nuclei,” , vol. 472, pp. L109–L114, Nov. 2017.

[11] B. Diemer, “COLOSSUS: A Python Toolkit for Cosmology, Large-scale Structure, and Dark Matter Halos,” , vol. 239, p. 35, Dec 2018.

[12] G. Despali, C. Giocoli, R. E. Angulo, G. Tormen, R. K. Sheth, G. Baso, and L. Moscardini, “The universality of the virial halo mass function and models for non-universality of other halo definitions,” , vol. 456, pp. 2486–2504, Mar. 2016.

[13] Planck Collaboration, P. A. R. Ade, N. Aghanim, M. Arnaud, M. Ashdown, J. Aumont, C. Baccigalupi, A. J. Banday, R. B. Barreiro, J. G. Bartlett, and et al., “Planck 2015 results. XIII. Cosmological parameters,” , vol. 594, p. A13, Sept. 2016.

[14] P. Behroozi, R. Wechsler, A. Hearin, and C. Conroy, “UniverseMachine: The Correlation between Galaxy Growth and Dark Matter Halo Assembly from z=0-10,” *ArXiv e-prints*, June 2018.

[15] X. Shen, P. F. Hopkins, C.-A. Faucher-Giguère, D. M. Alexander, G. T. Richards, N. P. Ross, and R. C. Hickox, “The Bolometric Quasar Luminosity Function at z = 0-7,” *arXiv e-prints*, p. arXiv:2001.02696, Jan. 2020.

[16] J. Aird, A. L. Coil, and A. Georgakakis, “X-rays across the galaxy population - II. The distribution of AGN accretion rates as a function of stellar mass and redshift.,” , vol. 474, pp. 1225–1249, Jan. 2018.

[17] P. F. Hopkins, G. T. Richards, and L. Hernquist, “An Observational Determination of the Bolometric Quasar Luminosity Function,” , vol. 654, pp. 731–753, Jan. 2007.